Field-Scale Impact of Relative Permeability Normalisation-Reference Consistency on CO_2 Injectivity Predictions

Bettina Jenei[1,*], *Semetei* Zhainakov[1], *Abdulrahman* Helal[2], *Wael* Al-Masri[3], and *Leonhard* Ganzer[1]

[1]Clausthal University of Technology, Institute of Subsurface Energy Systems, 38678 Clausthal-Zellerfeld, Germany
[2]SLB, AB13, Aberdeen, United-Kingdom
[3]Geological Survey of Denmark and Greenland (GEUS), Department of Geo-energy and Storage, 1350 Copenhagen K, Denmark

Abstract. Laboratory measurements have demonstrated that single-phase brine permeability (k_w) may be lower than Klinkenberg-corrected gas permeability (k_{gas}) in clean sandstone. For the dataset adopted in this study, $k_w/k_g=\alpha=0.60$, corresponding to k_w being approximately 40% lower than k_g(equivalently, k_g approximately 67% higher than k_w). When CO_2-brine drainage relative permeability is normalised to k_w following standard SCAL practice, CO_2 relative permeability values above unity may arise: for the implemented dataset, the k_g-normalised CO_2 endpoint of 0.98 corresponds to a k_w-normalised endpoint of $0.98/\alpha\approx1.633$. The implemented relative-permeability tables originate from the oil-brine simulation dataset of Maas et al. [1] and are applied here as a controlled proxy to isolate the field-scale consequence of permeability-reference consistency; the study does not constitute a site-specific CO_2-brine relative-permeability characterisation. Although both normalisation conventions yield identical flow profiles when applied consistently, a mismatch arises in practice when k_g-normalised k_r functions are combined with a k_w-based grid permeability field, reducing the represented effective phase permeability by the factor α = 0.60 across the full saturation range. This study quantifies the field-scale consequences of this normalisation-reference mismatch using a semi-synthetic homogeneous saline aquifer model in compositional fully implicit simulation, with a 1000-day post-injection forecast. Three simulation cases are compared: a mismatched formulation (Case A), an internally consistent gas-reference formulation (Case B), and an internally consistent brine-reference formulation with CO_2 relative permeability above unity introduced via direct simulator input editing (Case C). Cases B and C produce equivalent results, confirming the re-normalisation equivalence at field scale. Case A yields systematically lower injectivity, higher near-wellbore pressure buildup, and reduced CO_2 plume extent. Ensuring consistency between the SCAL normalisation reference and the reservoir-model permeability basis is a prerequisite for accurate injectivity forecasts.

1 Introduction & Literature Review

Hard-to-abate emission industries, including cement, steel, and chemical manufacturing, face limited options for deep decarbonisation beyond carbon dioxide capture and storage (CO_2 CCS) [2, 3]. As deployment scales toward commercially relevant injection volumes, the accuracy of field-scale reservoir simulation becomes critical for well design, pressure management, and regulatory compliance. Relative permeability functions derived from Special Core Analysis (SCAL) constitute the principal dynamic input to compositional reservoir simulations and directly govern predictions of injectivity, pressure buildup, and CO_2 plume migration [4, 5]. A substantial experimental literature on CO_2-brine relative permeability is available, covering sandstones, carbonates, low-permeability formations, and caprocks across a wide range of reservoir pressures and temperatures [6–26]. Steady-state co-injection corefloods and unsteady-state displacement tests interpreted by numerical history matching are both well established, with CT-based local saturation methods providing improved control over capillary end effects [7, 8, 10, 20]. Reported CO_2 drainage endpoint relative permeabilities range from approximately 0.4 to 0.8 in sandstones under standard conditions, rising toward the gas permeability under depressurisation or high-capillary-number flow [6, 9, 15]. Flow rate, capillary number, heterogeneity, wettability, CO_2 phase state, interfacial tension, hysteresis, geochemical alteration, and surfactant treatment have all been identified as controls on measured kr behaviour [1, 7, 10, 13, 16–19, 21]. Cyclic injection studies further show that water evaporation, salt precipitation, and imbibition hysteresis can alter injectivity over extended injection periods [16, 18].
Recent studies continue to expand CO_2-brine relative-permeability characterisation beyond conventional coreflood interpretation.

A tabulated summary of the literature data is found in Table 1.

* Corresponding author: bettina.jenei@tu-clausthal.de

Table 1. Tabulated summary of literature data

Ref.	Authors (year)	Rock/system	P (bar)/ T (°C)	Method	Key relevance	k_{ref}
[6]	Zuo, Krevor, Falta & Benson (2012)	Berea / Mount Simon sandstone	27.6–124 / 50	USS (depressurisn.)	Exsolved CO_2 kr (0.4–0.8); brine kr (0.04–0.08)	k_w
[7]	Reynolds & Krevor (2015)	Bentheimer / heterogeneous sandstone	103–207 / 38–91	SS (CT)	Heterogeneity and capillary-number scaling of kr	k_w
[8]	Perrin et al. (2009)	Reservoir rocks (Otway)	124 / 63	SS (CT)	Flow-rate dependence and core heterogeneity	k_w
[9]	Bachu (2013)	W. Canada sandstones (multiple)	80–230 / 35–75	USS	Injectivity, pressure build-up and kr in field context	k_w
[10]	Chen & DiCarlo (2016)	Berea sandstone; $scCO_2$–brine	103.4 / 20	USS (local)	Local saturation method; reduces end-effect bias	k_w
[11]	Busch & Mueller (2011)	Reservoir rocks and caprocks	Various	Protocol	Standardisation and measurement uncertainty	not explicitly stated
[12]	Czarnota et al. (2022)	Bluff/Entrada sandstones	228–241 / 85–89	SS	Acoustic monitoring coupled to kr measurement	k_w
[13]	Akbarabadi & Piri (2013)	Berea/Nugget sandstones	34–110 / 20–55	SS + USS	Drainage/imbibition hysteresis; trapping curves	k_w
[14]	Berg, Oedai & Ott (2013)	Berea sandstone	100 / 45	USS (CT)	Mass transfer, dry-out and dissolution effects	k_w
[15]	Jeong, Lee, Ki, Huh & Park (2017)	CO_2/brine; sandstone	80–150 / 35–60	SS + USS	IFT, viscosity ratio and hysteresis effects on kr	k_w
[16]	Bachu & Bennion (2008)	Sandstone, carbonate, shale	86–270 / 35–75	USS	P, T, salinity, IFT and pore-size effects on kr	k_w
[17]	Sun et al. (2021)	Feldspar/dolomite-rich tight sandstone	150–250 / 44–64	SS	Geochemical alteration of kr after CO_2–rock reaction	k_w-like basis
[18]	Jeong et al. (2021)	CO_2/brine; sandstone	80–150 / 35–60	USS	Flow-rate effect on endpoint kr and residual brine saturation	k_w
[19]	Bennion & Bachu (2006)	Wabamun sandstone/carbonate	86–270 / 35–75	USS	IFT and pore-size distribution effects on kr and Pc (SPE-99325)	Probably k_w(Not explicitly stated)
[20]	Reynolds, Blunt & Krevor (2014)	Bentheimer sandstone	103–207 / 38–91	SS (CT)	Viscous-limit scaling; intrinsic vs apparent kr	k_w
[21]	Seok et al. (2023)	Berea sandstone with surfactant	100 / 40	SS (CT)	Surfactant increases CO_2 kr by ≥56% vs baseline	k_w
[22]	Bennion & Bachu (2007)	Shale/anhydrite caprocks	86–270 / 35–75	USS	Caprock kr; containment and leakage risk (SPE-106995)	k_w
[23]	Farokhpoor et al. (2014)	Svalbard low-perm sandstone	~100 / 40	SS + USS	Low-k sandstone kr; geochemical reactions	k_w-like basis
[24]	Moore et al. (2021)	Reactive/non-reactive rocks	~97 / 63	USS (CT)	Rapid kr determination; matrix dissolution effect	k_w
[25]	Bennion & Bachu (2005)	WCSB sequestration sandstones	80–230 / 35–75	USS	Early WCSB drainage kr dataset (SPE-95547)	k_w
[26]	Chen, Kianinejad & DiCarlo (2014)	Berea sandstone; sc CO_2–brine	103.4 / 20	SS	Endpoint kr ≈ 0.4; long-core end-effect mitigation (SPE-169137)	k_w
[35]	Ahmed et al. (2024)	Berea sandstone; CO_2/brine	1500 psi / 150°F	Experimental + ML	CO_2 storage exposure effect on CO_2-brine kr; ML prediction of krw/krg	not explicitly stated
[36]	Chai et al. (2026)	Reservoir sandstone; CO_2/brine	10.3 MPa / 60°C for SCAL; 8 MPa / 50°C for DRP	SS + CT + DRP/PNM	Multiscale SCAL–digital-rock workflow; drainage, imbibition and capillary trapping	carbonated-brine permeability
[37]	Walls et al. (2025)	CO_2/brine	not verified from abstract	Multi-rate USS	Multi-rate unsteady-state method for CO_2-brine relative permeability; comparison with steady-state method	not explicitly stated

Ahmed et al. [35] investigated CO_2-brine relative permeability in Berea sandstone before and after CO_2 storage exposure and combined experimental observations with machine-learning prediction of k_{rw} and krg. Chai et al. [36] presented an integrated SCAL–digital-rock workflow combining steady-state CO_2-brine relative permeability, CT-based saturation monitoring, micro-CT imaging, and pore-network modelling to characterise drainage, imbibition, and capillary trapping in reservoir sandstone. Walls et al. [37] further demonstrated a multi-rate unsteady-state approach for CO_2-brine relative-permeability measurement. These recent studies reinforce the importance of relative permeability for CO_2 injectivity, plume migration, and trapping, but do not address the field-scale impact of inconsistent normalisation between SCAL data and reservoir-model permeability. The k_{ref} column in Table 1 above reflects the normalisation reference documented in, or inferred from, the cited publications. While the majority of studies report kw as the stated or implied reference for their laboratory measurements, none of the cited studies considered the choice of permeability reference (kw versus kg) or the consequences of inconsistent normalisation in reservoir simulation workflows as a modelling parameter. This gap motivates the present study. Despite this breadth, the absolute-permeability reference used to normalise relative permeability functions is rarely documented in published datasets, making retrospective assessment of normalisation conventions difficult without access to the original raw data.

A critical but underappreciated source of systematic bias in translating laboratory data to reservoir simulators is the choice of reference permeability used to normalise measured k_r curves. Maas et al. [1] demonstrated that the Klinkenberg-corrected gas permeability (k_{gas}) systematically exceeds single-phase brine permeability (k_w) in clean sandstone. For the OBKN sandstone investigated experimentally, they reported $k_w/k_g \approx 0.70$, attributing the reduction to ionic double-layer forces at the charged quartz surface. Their illustrative simulation dataset (Table 15) adopted $k_w/k_g=0.60$ to demonstrate the re-normalisation equivalence; this value is used in the present study because the corresponding tabular k_r data are applied directly. For this dataset, k_g is approximately 67% higher than k_w (equivalently, k_w is approximately 40% lower than k_g). When CO_2-brine drainage relative permeability is normalised to k_w following standard SCAL practice, the CO_2 endpoint at irreducible water saturation approaches $k_g/k_w=1/\alpha \approx 1.67$, where $\alpha=k_w/k_g$ denotes the permeability ratio. For the implemented dataset, the gas-normalised CO_2 endpoint is 0.98, the corresponding brine-normalised CO_2 endpoint is $0.98/\alpha \approx 1.633$.

Commercial reservoir simulators typically restrict relative permeability inputs to values within [0, 1] through their graphical interfaces, although in the Intersect™ implementation used here the complete brine-normalised curve, including $k_r > 1$, was introduced through direct editing of the simulator input definition. Maas et al. [1] confirmed at core scale that both normalisation conventions yield identical flow profiles when the reference permeability and k_r curves are used consistently. This equivalence is broken when a mismatch arises between the normalisation reference of the k_r functions and the absolute-permeability basis of the simulation grid. The core-scale consequences of normalisation choice are now established, but the field-scale impact of a normalisation-reference mismatch has not been systematically quantified in the published literature. Near the injection well, continuous drainage drives water saturation toward the irreducible value, so the high-CO_2-saturation region of the k_r curve is visited most frequently and for the longest duration. The present study addresses this gap by implementing a semi-synthetic homogeneous saline aquifer model in Intersect™ to compare three otherwise identical simulation cases: (i) a mismatched formulation combining a k_w-based grid permeability field with k_g-normalised k_r functions (Case A); (ii) an internally consistent gas-reference formulation with k_g grid permeability and k_g-normalised k_r (Case B); and (iii) an internally consistent brine-reference formulation with k_w grid permeability and k_w -normalised k_r including CO_2 endpoints above unity (Case C). Differences in well injectivity, near-wellbore and far-field pressure, CO_2 plume geometry, and contacted pore-volume fraction are quantified over the injection period and a 1000-day post-injection forecast.

1.1 Summary of the $k_{gas}>k_{brine}(k_w)$problem

Darcy [27] defined permeability as an intrinsic property of the porous medium, independent of the saturating fluid. Klinkenberg [28] showed that gas permeability measured at finite pore pressures is higher than the true value due to gas slippage at pore walls, and proposed a correction to recover the liquid-equivalent permeability. After applying this correction, gas and liquid permeabilities are expected to be equal for clean, non-reactive rocks. In practice, however, k_w is systematically lower than k_g even after the Klinkenberg correction is applied, and even in rocks where clay swelling and fines migration can be excluded. Reductions of 25-50% are common in clean sandstones [1, 29, 30]. Maas et al. [1] demonstrated through experiments on inert ceramic plugs and clean OBKN sandstone (94% quartz, 5% kaolinite) that this discrepancy is reproducible and independent of brine salinity and equilibration time, attributing it to ionic double-layer forces at the charged quartz surface. The mean experimental ratio k_w/k_g was approximately 0.70 for OBKN sandstone, statistically significant at the 0.1% level. Their illustrative simulation example (Table 15) adopted $k_w/k_g= 0.60$ to demonstrate the re-normalisation equivalence using paired k_r datasets; this value is used in the present study because the corresponding tabular k_r data are applied directly. In clay-bearing reservoir rocks, where ionic surface interactions are stronger, values of α may be considerably lower.

1.2 Gap in the literature: core-scale effect established

The equivalence of the two internally consistent normalisation conventions was demonstrated at core scale by Maas et al. [1]. Two related but distinct gaps emerge for field-scale application. First, explicit documentation of the normalisation reference is absent from the vast majority of published SCAL datasets, making it impossible to retrospectively assess whether existing reservoir models combine k_r functions with a consistent or mismatched grid permeability basis. Second, no published study has systematically quantified how a normalisation-reference mismatch propagates through a compositional reservoir simulator to affect well injectivity, pressure evolution, and CO_2 plume geometry at field scale. This is the central contribution of the present work.

2 Theoretical Background

2.1. The k_{gas}/k_{brine} discrepancy and its origin

Klinkenberg [28] demonstrated that apparent gas permeability measured at finite pore pressures exceeds the true liquid-equivalent value due to gas slippage at pore walls, a phenomenon arising when the mean free path of gas molecules becomes comparable to the pore throat diameter. Applying the Klinkenberg correction removes the slippage contribution and recovers the true intrinsic permeability from gas measurements. For clean, non-reactive rocks saturated with non-polar liquids, the corrected gas permeability and the liquid permeability converge to the same value.

When brine is used as the saturating fluid, however, a reproducible discrepancy persists: k_w is systematically lower than k_g by 25-50% in clean sandstones, and potentially more in clay-bearing formations [1, 29, 30]. Several mechanisms can suppress brine permeability below the true intrinsic value: clay swelling and fines migration, structured water layers adsorbed onto mineral surfaces, ion-specific surface interactions, and osmotic effects. None of these mechanisms act in the case of a non-polar gas such as helium or nitrogen. Maas et al. [1] isolated the surface-ionic component of this suppression through systematic experiments on inert ceramic plugs (100% Al_2O_3) and clean OBKN sandstone. The ceramic plugs showed $k_w=k_g$ within statistical uncertainty, confirming that the discrepancy is not an instrumental artefact. The OBKN sandstone showed a mean experimental ratio $k_w/k_g\approx0.70$ (statistically significant at the 0.1% level, independent of brine salinity and equilibration time), which Maas et al. attributed to ionic double-layer forces between the negatively charged quartz surface and the ions in the brine. The illustrative simulation example in their Table 15 adopted $k_w/k_g=0.60$ to demonstrate the re-normalisation equivalence using paired k_r datasets; this value is used in the present study because the corresponding tabular k_r data are applied directly. The k_g/k_w gap is a physical property of the brine-rock system rather than a laboratory artefact.

2.2 Consequences for relative permeability normalisation

Relative permeability of phase i is defined as:

$$k_{ri} = Keffi_i / Kref \qquad (1)$$

where $KEFF_i$ is the effective permeability to phase i at a given saturation and Keffis the chosen reference absolute permeability. The reference permeability sets the scale of the entire k_r curve: a change in Krefrescales all k_r values by the inverse factor. In standard SCAL practice for CO_2-brine drainage, Kref=k_w. The brine-normalised CO_2 endpoint approached at Swirr → $Swirr_i$ is $k_g/k_w=1/\alpha\approx1.67$. For the implemented dataset, the gas-normalised CO_2 endpoint at Swirr = 0.05 is 0.98, so the corresponding brine-normalised CO_2 endpoint is:

$$krco_2(Swir = 0.05) = 0.98/\alpha\approx1.633 \qquad (2)$$

This value exceeds unity. The constraint $0 \le k_{ri} \le 1$ in conventional reservoir simulators derives from the classical multiphase extension of Darcy's law:

$$u_i = -(k \cdot k_{ri} / \mu_i)\ \nabla P_i \qquad (3)$$

in which each phase is assumed to flow under its own pressure gradient and to interact with the other phase only by occupying part of the pore space. Generalised formulations of two-phase flow developed by Whitaker [33] and others, comprehensively reviewed by Ayub and Bentsen [34], include cross-coupling terms representing momentum transfer through the fluid-fluid interface:

$$u_i = -(k_{ii} / \mu_i)\ \nabla P_i - (k_{ij} / \mu_j)\ \nabla P_j \qquad (4)$$

where k_{ij} are off-diagonal coupling coefficients. The present simulations use the diagonal formulation of Eq. 3 and do not separately quantify cross-coupling or interfacial momentum-transfer effects. The discussion of Eq. 4 is provided as theoretical context for the existence of relative permeability values above unity; the field-scale results presented in subsequent sections evaluate only the consequence of applying relative permeability functions with a normalisation reference inconsistent with the absolute-permeability basis of the simulation grid.

Commercial reservoir simulators typically restrict direct entry of $k_{ri} > 1$ through their graphical interfaces because the cross-coupling terms are not represented explicitly. In the Intersect™ implementation used in this study, the complete brine-normalised CO2 curve, including its endpoint of 1.633, was introduced through direct editing of the simulator input definition. No endpoint capping is applied in any of the three simulation cases. If instead $K_{ref}=k_g$, the gas-normalised CO2 endpoint approaches $k_g/k_g = 1.0$ in the limit; the implemented value is 0.98 at $S_{wirr} = 0.05$.

2.3 Re-normalisation equivalence, and its limits

The CO_2 Darcy flux under the diagonal formulation depends on the product $k_{ref}\times k_{ri} = K_{effi}$. When k_{ref} and k_{ri} are rescaled consistently by α and 1/α respectively, this

product is unchanged and the simulated flux is identical in both formulations:

$$Kg \times k_{ri}(g) = (Kw/\alpha) \times (\alpha\, k_{ri}) = Kw \times k_{ri}(w) = Keffi \quad (5)$$

Maas et al. [1] verified this equivalence at the core scale using the SCORES simulator, demonstrating identical production profiles, differential pressures, and saturation distributions for both conventions when $k_r > 1$ was permitted. This equivalence is broken when the normalisation reference used for the k_r curves does not match the absolute-permeability basis of the simulation grid. In Case A, the k_g-normalised k_r functions are combined with a k_w-based grid, so the represented effective phase permeability is $k_w \times k_{ri}^{(gas)} = \alpha \times Keffi$. For $\alpha = 0.60$, this represents a 40% reduction in represented effective phase permeability relative to the internally consistent Cases B and C across the full saturation range, for both the CO_2-rich and aqueous phases. At the core scale, the effect of a normalisation-reference mismatch on integrated quantities such as cumulative production may be modest. At field scale, the mobility reduction introduced by the mismatch affects the entire aquifer volume traversed by the pressure wave during injection, and additionally affects the near-wellbore CO_2-rich region that develops progressively during drainage. Near-wellbore pressure feedback couples the injectivity deficit to the global pressure response: a reduction in effective phase mobility at the well increases the bottomhole pressure, which under a pressure-constrained schedule reduces the injection rate and propagates the near-wellbore bias into the far-field pressure footprint and plume geometry. These field-scale mechanisms motivate the simulation analysis presented in Sections 5 and 6.

3 Reservoir Model and Simulation Setup

3.1 Static Model

A semi-synthetic saline aquifer model was constructed for proof-of-concept purposes, designed to isolate the impact of relative permeability normalisation on field-scale CO_2 injection performance without confounding site-specific factors. The model represents a generic deep saline aquifer typical of North Sea geological CO_2 storage targets. The model domain has lateral dimensions of 1000*1000m and a net interval thickness of 10m, discretised into a 100*100*20 Cartesian grid with lateral cell dimensions of 10 × 10 m and vertical cell thickness 0.5 m, yielding approximately 0.2 million active grid cells. Porosity is uniformly assigned as 0.184, representative of clean to moderately consolidated sandstones. Absolute permeability is uniform with a value of k_w= 100 mD; the corresponding $k_g = k_w/\alpha$ = 166.7 mD is used to populate the grid in Case B. The ratio $\alpha = 0.60$ is adopted from the illustrative simulation dataset of Maas et al. [1] (their Table 15), which differs from the experimentally measured mean ratio of kw/kg ≈ 0.70 for OBKN sandstone reported in the same study; $\alpha = 0.60$ is used here because the corresponding tabular k_r data are applied directly. Vertical-to-horizontal permeability anisotropy is kv/kh = 0.1. The structure is horizontal to exclude the influence of structural dip on lateral plume migration; vertical buoyancy segregation of CO_2 within the aquifer thickness remains represented. A perfectly sealing caprock bounds the model above and closed boundary conditions are applied at all lateral boundaries, with no regional pressure support from the surrounding aquifer. The aquifer is initially fully brine-saturated with $Swirr_{,o} = 1.0$; irreducible water saturation $Swirr_i$ is a drainage k_r endpoint and is not used as the initial reservoir condition.

3.2 Fluid and thermodynamic properties

Reservoir conditions representative of a 1200 m deep CO_2 storage formation are applied: temperature T = 55 °C and hydrostatic initial average pressure Pi = 135 bar. Under these conditions, CO_2 is supercritical with a density of approximately 660 kg/m³ and a dynamic viscosity of approximately 0.055 mPa·s. Formation brine has a salinity of 179,200 ppm NaCl with a density of 1.133 g/cm³ and a viscosity of 1.1 cP at reservoir conditions. Phase behaviour is described using a calibrated Soave-Redlich- Kwong (SRK) equation of state [31]. CO_2 solubility in brine is modelled using the mutual solubility model of Spycher and Pruess [32], which accounts for CO_2 dissolution into the aqueous phase and water vaporisation into the CO_2-rich phase as a function of pressure, temperature, and salinity. The model is initialised hydrostatically with a salinity-dependent brine density to establish a consistent pressure-depth profile prior to injection. No mineralisation reactions are included, as the study focuses on injectivity and plume dynamics over the injection period. Capillary pressure is supplied as a tabular Pc(Swirr) function was not applied identically in all three cases; no Leverett-J scaling is applied. This avoids the dependence on grid permeability that would otherwise affect the equivalence between Cases B and C [1].

3.3 Injection scenario

A single vertical well is completed across the full aquifer interval at the centre of the model. CO_2 is injected at a constant target rate of 1000 Sm³/day (approximately 1.85 t/day at standard conditions) for 20 years, subject to a maximum bottomhole pressure (BHP) constraint, corresponding to 90% of the estimated minimum in-situ stress to avoid hydraulic fracturing. When the BHP limit is reached, the simulation switches to pressure-controlled injection at Pmax. Following shut-in, the simulation is continued for a further 1000 days to track plume redistribution, overpressure equilibration within the closed model domain, and CO_2 dissolution into formation brine. Residual trapping is not represented because no imbibition or hysteresis formulation was included.

3.4 Simulator settings

Simulations are performed using Intersect™ (SLB), a fully implicit isothermal compositional reservoir

simulator. The fully implicit formulation ensures unconditional stability across the wide range of time steps required to span the 1000-day post-injection forecast. The CO_2-brine system is represented as a two-component, two-phase system with phase partitioning governed by the calibrated SRK equation of state [31] and the Spycher and Pruess [32] solubility model described above. The geological grid contains 0.2 million active cells (Section 3.1). Time-step sizes were selected based on convergence testing to confirm independence of the injection-period results from the temporal discretisation, and to verify that cumulative mass-balance error remained below the allowed threshold over the full 1000-day forecast. Relative permeability input handling differs between the three cases. In Cases A and B, all k_r values are below or equal to 1.0 by construction (k_g-normalised functions) and no special input handling is required. In Case C, the k_w-normalised CO_2 curve has an endpoint of $0.98/\alpha \approx 1.633$, which exceeds the value accepted through the standard graphical interface of Intersect™. The complete curve was therefore introduced through direct editing of the simulator input definition. No endpoint capping is applied in any of the three cases; the distinction between the cases is entirely in the grid permeability basis and the normalisation reference of the k_r functions.

4 Relative Permeability Input Functions

4.1 Laboratory data

The relative permeability tables used in this study are taken directly from the simulation dataset of Maas et al. [1] (their Table 15), which was developed to demonstrate the re-normalisation equivalence at core scale for a water-wet OBKN-sandstone oil-brine drainage system. The dataset is applied here as a controlled proxy for the dynamic mobility functions of the CO_2-brine system. The objective is to isolate the field-scale consequence of permeability-reference consistency, not to reproduce CO_2-specific experimental k_r behaviour. The ratio $\alpha = k_w/k_g = 100/166.7 \approx 0.60$ from that dataset is used directly. Curves are supplied to the simulator as tabular inputs with eleven saturation points spanning Swirrc = 0.05 to Swirr,max = 0.99; no Corey parameterisation is applied. The used tabular k_r values for both normalisations are shown in Table 2.

4.1.1 Case A: normalisation-reference mismatch (k_w= 100 mD grid, k_g-normalised k_r)

In Case A, the grid absolute permeability is k_w= 100 mD but the k_r functions are k_g-normalised, giving a CO_2 endpoint of 0.98 at Swirr = 0.05 and a brine endpoint of 0.50 at Swirr = 0.99. The product $K^{gr_i d} \times k_r$ therefore underrepresents the true effective phase permeability by the factor $\alpha = 0.60$ across the full saturation range, for both the CO_2-rich and aqueous phases. This configuration corresponds to a practical workflow in which k_g-normalised SCAL data are applied to a reservoir model whose permeability field is based on k_w without transformation of the grid permeability basis.

4.1.2 Case B: internally consistent gas-reference formulation, kg-normalised k_r (Maas et al. recommendation)

In Case B, the grid permeability is k_g=166.7 mD and the k_r functions are k_g-normalised, giving a CO_2 endpoint of 0.98 at Swirr = 0.05 and a brine endpoint of 0.50 at Swirr = 0.99. The product $K^{gr_i d} \times k_r$ correctly represents the true effective phase permeability.

4.1.3 Case C: internally consistent brine-reference formulation, kw-normalised k_r with $k_{r,CO_2} > 1$

In Case C, the grid permeability is k_w= 100 mD and the k_r functions are k_w-normalised, giving a CO_2 endpoint of 1.633 at Swirr = 0.05 and a brine endpoint of 0.833 at Swirr = 0.99. The product $K^{gr_i d} \times k_r$ again correctly represents the true effective phase permeability. Cases B and C are therefore mathematically equivalent representations of the same effective phase permeability. Table 3 summarises the input parameters for all three cases.

Table 2. Tabular relative permeability data adopted from Maas et al. [1] (Table 15). The k_g-normalised columns are used in Cases A and B; the k_w-normalised columns are used in Case C.

Sw	krw	kro	krw	kro
0.05	0	0.98	0	1.633333
0.144	0.000032	0.737362	0.000053	1.228937
0.238	0.00058	0.536499	0.000966	0.894165
0.332	0.003183	0.374103	0.005306	0.623505
0.426	0.010657	0.246737	0.017761	0.411228
0.52	0.027205	0.150815	0.045341	0.251358
0.614	0.058507	0.082564	0.097511	0.137606
0.708	0.111785	0.037971	0.186308	0.063285
0.802	0.195861	0.012706	0.326435	0.021177
0.896	0.32121	0.001955	0.53535	0.003259
0.99	0.5	0	0.833333	0

Table 3. Relative permeability and grid permeability inputs for Cases A, B, and C. Tabular k_r values from Maas et al. [1].

Parameter	Case A	Case B	Case C
Grid absolute permeability (mD)	k_w=100	k_g=166.7	k_w=100
k_r normalisation reference	k_g	k_g	k_w
$\alpha=k_w/k_g$	0.60	0.60	0.60
CO_2 endpoint k_rco_2 @ Sw = 0.05	0.980	0.980	1.633
Brine endpoint k_r^w at $Swir_r$ = 0.99	0.500	0.500	0.833
Reference consistency	Mismatched	Consistent	Consistent
Represented effective phase permeability	0.60 Keffi	Keffi	$Keffi_i$

4.2 Isolation of the normalisation effect

All inputs other than the k_r curves and the absolute permeability field are identical among Cases A, B, and C: capillary pressure curves, PVT properties, grid geometry, rock compressibility, boundary conditions, and injection schedule are unchanged. Cases B and C are expected to produce identical results, providing an internal verification of the normalisation transformation and the simulator input workflow.

Case A quantifies the field-scale consequence of the normalisation-reference mismatch.

5 Results

The following subsections present the simulation results. Results first verify the equivalence of the two internally consistent formulations (Cases B and C), then quantify the effect of the normalisation-reference mismatch (Case A vs Cases B and C).

5.1 Verification of the internally consistent formulations and effect of the normalisation-reference mismatch on injectivity and pressure

Figure 1 shows the simulated CO_2 injection rate and bottomhole pressure (BHP) as a function of time for Cases A, B, and C.

Cases B and C are expected to produce identical results, verifying that the normalisation transformation has been correctly implemented and that CO_2 relative permeability values above unity in Case C represent physically consistent phase mobility when combined with the k_w -based grid. Under rate-controlled injection, Cases B and C are expected to sustain the target injection rate of 1000 Sm^3/day throughout the 20-year injection period, while Case A, with its reduced represented effective phase permeability, reaches the BHP limit at approximately [tA] years, transitioning to pressure-controlled injection. The cumulative CO_2 mass stored in Cases B and C exceeded Case A by [X]% at the end of injection. [Insert quantitative results from final simulation output, including maximum difference between Cases B and C and the magnitude of the Case A deficit relative to Cases B/C.]

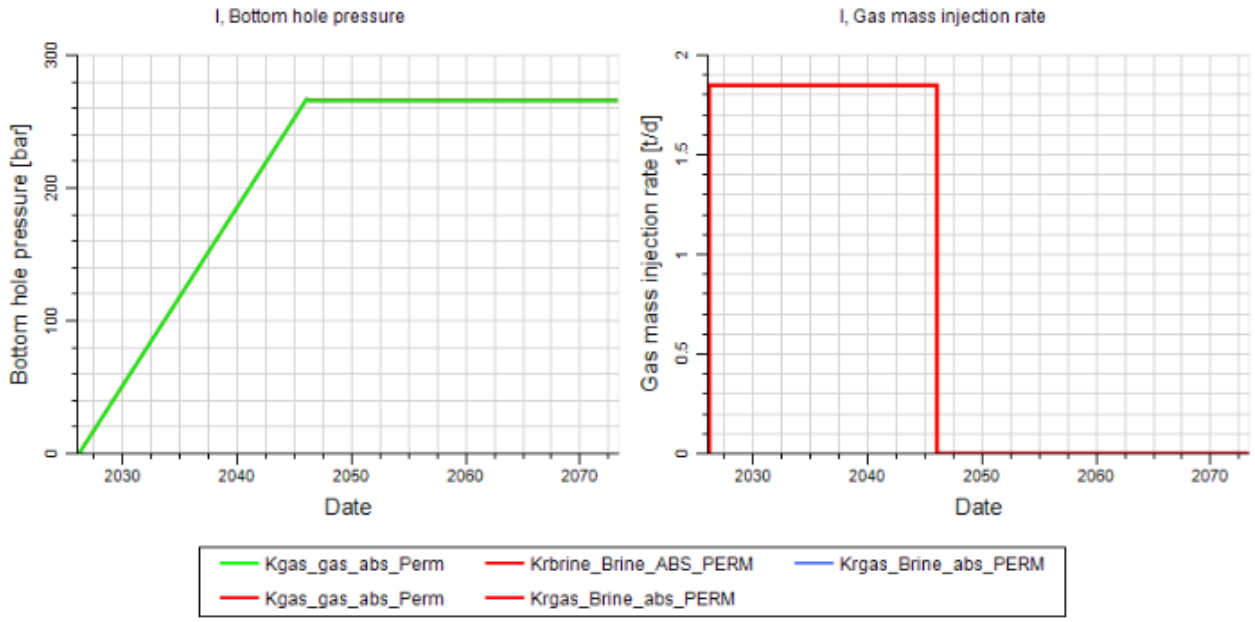

Fig. 1. CO_2 injection rate and bottomhole pressure (BHP) as a function of time for Cases A, B, and C, showing overlap of Cases B and C and the deficit in Case A.

5.2 CO_2 plume migration

Figures 2-5 show CO_2 saturation cross-sections at the end of injection and at the end of the 1000-day forecast for all three cases. By the end of injection, the CO_2 plume in Cases B and C had a lateral extent of [X] m compared to [X] m in Case A. Vertical buoyancy segregation drove preferential migration toward the top of the aquifer in all cases. Post-injection, the plume continued to redistribute laterally under buoyancy and dissolved progressively into the formation brine. Dissolved CO_2 accounted for [X]% and [X]% of total stored CO_2 mass in Case A and Cases B/C respectively at the end of the 1000-day forecast. Residual trapping was not represented in the model, as no imbibition or hysteresis formulation was included.

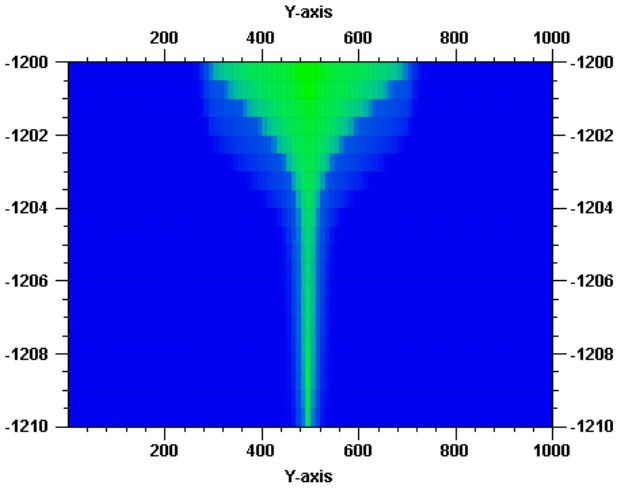

Fig. 2. Case A CO_2 plume at the end of 20 years injection

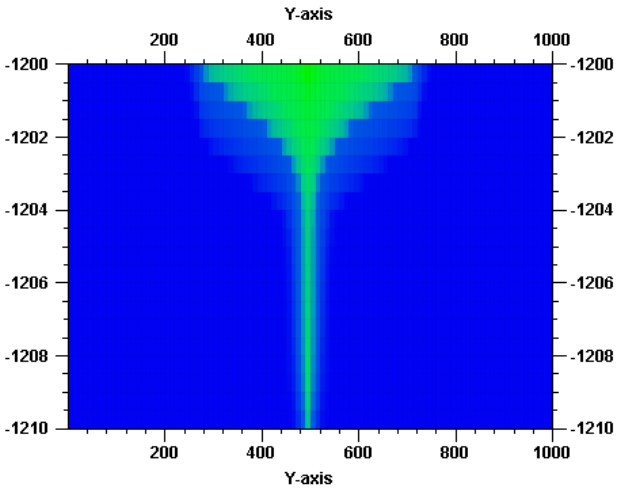

Fig. 3. Case B and C CO_2 plume at the end of 20 years injection

By the end of injection, the CO_2 plume in Cases B and C had a lateral extent of X m compared to X m in Case A. Gravity segregation drove preferential migration toward the top of the aquifer in all cases. Post-injection, the plume continued to migrate laterally under buoyancy and dissolved progressively into the formation brine. Dissolved CO_2 accounted for X % and X % of total stored CO_2 mass in Case A and Cases B/C respectively at the end of the 1000-day forecast period. Residual trapping was not represented in the model, as no hysteresis formulation, therefore no imbibition curve was included.

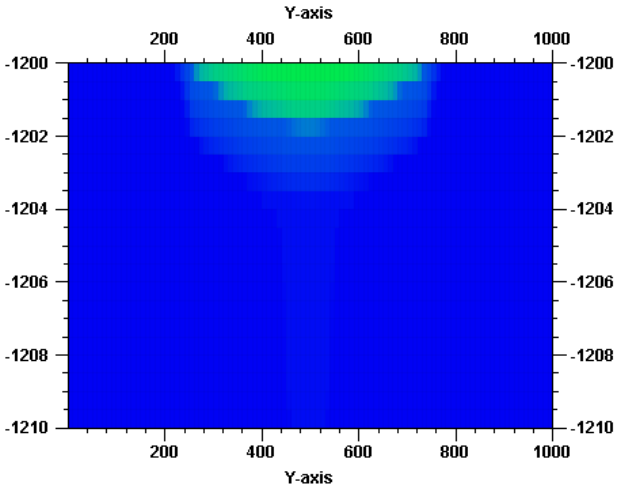

Fig. 4. Case A CO_2 plume at the end of post injection

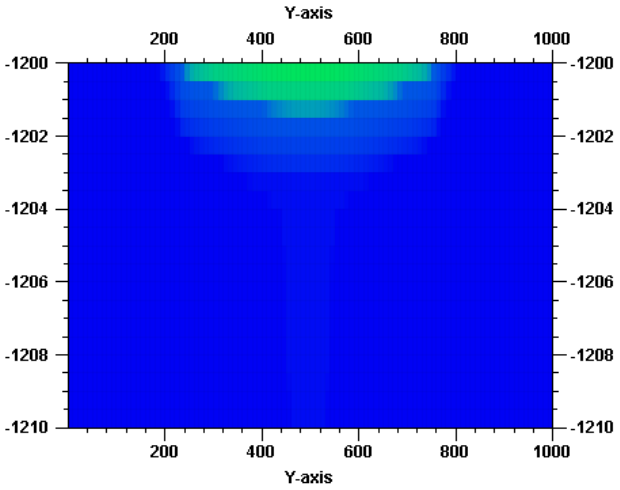

Fig. 5. Case B and C CO_2 plume at the end of post injection

6 Discussion

The simulation results confirm that normalisation-reference consistency between SCAL data and the reservoir-grid permeability is a first-order modelling parameter in CO_2 injection simulation. The equivalence of Cases B and C verifies that CO_2 relative permeability values above unity in the brine-normalised representation are not physically anomalous; they are the correct values when the corresponding k_w -based grid permeability is used. The underestimation of effective phase permeability in Case A arises from combining k_g-normalised k_r functions with a k_w -based grid, and this bias operates across the full saturation range for both phases, not only in the CO_2-dominated near-wellbore zone.

The equivalence of Cases B and C demonstrated here at field scale confirms the re-normalisation result of Maas et al. [1] at core scale: the choice of reference permeability system is arbitrary provided it is applied consistently to both the k_r functions and the grid permeability field. The magnitude of the mismatch bias in Case A scales with $\alpha = k_w/k_g$, which the dataset used here assigns the value 0.60. In clay-bearing reservoir rocks, where this ratio is typically lower, the field-scale bias would be proportionally greater. The bias accumulates over the injection period as an increasing fraction of the aquifer transmissibility is controlled by the mismatched k_r product.

The practical consequences for CO_2 CCS projects are significant. Applying k_g-normalised SCAL data to a reservoir model whose permeability field is based on k_w will systematically underestimate CO_2 injection rates, potentially leading to conservative well design, underutilised geological CO_2 storage capacity, and unnecessary additional injection wells. Pressure footprint assessments will overestimate the zone of influence, which may result in overly restrictive injection schedules and conservative caprock risk assessments.

A practical correction is available within standard SCAL and reservoir-modelling workflows. The ratio $\alpha=k_w/k_g$ can be computed from routine core analysis measurements already performed in most programmes. Either the k_r curves should be re-normalised from the k_g basis to the k_w basis before being used with a k_w grid (producing Case C-style inputs including endpoints above unity), or the grid permeability field should be scaled to k_g before Case B-style inputs are applied. Both approaches eliminate the normalisation-reference mismatch without any additional SCAL measurements. Explicit documentation of the normalisation reference used in SCAL reporting is a prerequisite for applying either correction.

A limitation of the present study is the use of a homogeneous semi-synthetic model with a single value of α adopted from the simulation example of Maas et al. The implemented k_r tables originate from an oil-brine drainage dataset and are applied as a controlled proxy; the study therefore does not constitute a site-specific CO_2-brine characterisation. Future work should evaluate heterogeneous realisations, a range of α values representative of different rock types, the interaction between normalisation-reference consistency and structural or stratigraphic heterogeneity, and the inclusion of hysteresis to quantify long-term residual trapping.

7 Conclusions

The following conclusions are drawn from this proof-of-concept study:

1. Normalisation-reference consistency between SCAL-derived k_r functions and the absolute permeability basis of the simulation grid is a first-order modelling parameter in CO_2 injection simulation. The mathematical equivalence of brine-normalised and gas-normalised conventions holds only when the chosen reference permeability is applied consistently to both the k_r curves and the grid permeability field.
2. Cases B (k_g-normalised k_r with k_g grid) and C (k_w-normalised k_r with k_w grid, including CO_2 endpoints above unity) produce equivalent simulation results, confirming that k_r values above unity in the brine-normalised representation do not represent anomalous phase mobility when used with the corresponding brine-based absolute permeability. The equivalence demonstrated by Maas et al. [1] at core scale is reproduced at field scale.
3. The normalisation-reference mismatch in Case A (k_g-normalised k_r with k_w grid) reduces represented effective phase permeability by the factor $\alpha = 0.60$ across the full saturation range. This yields lower injectivity, higher near-wellbore pressure buildup, and reduced CO_2 plume extent relative to the internally consistent formulations.
4. Explicit documentation of the normalisation reference used in SCAL reporting and consistent application of this reference in the reservoir model are prerequisites for accurate injectivity forecasts and pressure management. The correction requires only $\alpha=k_w/k_g$ from routine core analysis and can be applied by re-scaling either the k_r curves or the grid permeability field, without additional SCAL measurements.

8 Limitations and Future Work

The present results are obtained from a homogeneous proof-of-concept model that deliberately isolates the normalisation-reference effect. The simplicity of this controlled design should not be interpreted as evidence that the bias is small in practice. Because the effect of a reference-consistency mismatch is coupled to CO_2 phase mobility, and CO_2 plume position is in turn coupled to different phase mobilities, the magnitude of the bias depends strongly on factors that influence plume position and on factors that are themselves influenced by it. Systematic sensitivity analyses are therefore required before the present conclusions can be extrapolated to site-specific assessments.

In a homogeneous model with a single value of α, the normalisation-reference mismatch introduces a uniform mobility scaling across the entire domain. In heterogeneous reservoirs where α varies spatially between rock types, as expected in layered or facies-controlled systems with varying clay content, the mismatch scaling would itself be spatially variable, potentially producing differential injectivity responses and altered plume steering that cannot be captured by a single uniform correction factor. Sensitivity analyses across a range of α values representative of different lithofacies are therefore required before the present conclusions can be extrapolated to heterogeneous settings.

Sensitivity analyses varying permeability, pressure, depth, or dip angle within an already inconsistently formulated scenario would not yield generalisable conclusions, as the magnitude of any observed bias would be case-dependent and could not be extrapolated beyond the specific model configuration. The appropriate correction, ensuring consistency between the

normalisation reference and the grid permeability basis, eliminates the mismatch entirely, rendering sensitivity analysis of the inconsistent formulation unnecessary. Future sensitivity work is therefore most meaningful when applied to the consistently formulated Cases B and C, to characterise how geological and fluid-property uncertainty modulates injectivity and plume geometry independently of the normalisation-reference effect.

Future work should evaluate: (i) geological heterogeneity and the associated parameter uncertainty; (ii) a range of drainage relative-permeability characteristics, such as shapes, including variation of the irreducible water saturation S_{wirr} and residual CO_2 saturation S_{gr} for imbibition; (iii) capillary-pressure functions, including Leverett-J formulations in which the reference-consistency requirement extends to the capillary-pressure entry; (iv) hysteresis and imbibition curves to represent residual trapping; (v) alternative reservoir geometries, dip angles, and boundary conditions; and (vi) variations in brine salinity with full activation of the Spycher and Pruess [32] solubility model. The solubility is especially important in low salinity cases because there the solubility trapping is more dominant in the post injection phase. Each of these factors either influences the location of the CO_2 plume or is influenced by it, and therefore modulates the field-scale consequence of normalisation-reference inconsistency.

Nomenclature

α	Permeability ratiokw/kg (-)
BHP	Bottomhole pressure (bar)
CCS	Carbon dioxide storage
Keffi	Effective permeability to phase i (mD)
Kg	Klinkenberg-corrected gas permeability (mD)
Kh	Horizontal permeability (mD)
Kref	Reference absolute permeability (mD)
k_r	Relative permeability (-)
k_r,	CO_2CO_2 relative permeability (-)
krw	Brine relative permeability (-)
kv	Vertical permeability (mD)
kw	Single-phase brine permeability (mD)
μi	Dynamic viscosity of phase i (mPa·s)
Pi	Initial reservoir pressure (bar)
Pc	Capillary pressure (bar)
SCAL	Special Core Analysis
Sgr	Residual CO_2 saturation (-)
SRK	Soave-Redlich-Kwong equation of state
Sw	Water saturation (-)
Swirr	Irreducible water saturation (-)
T	Reservoir temperature (°C)
Ui	Darcy flux of phase i (m/s)

References

1. J.G. Maas, D. Santonico, A. Hebing, N. Springer, SCA2025-1037 (2025).
2. S.M. Benson, D.R. Cole, Elements, 4(5), 325–331 (2008).
3. S. Bachu, Energy Conversion and Management, 41(9), 953–970 (2000).
4. R.H. Brooks, A.T. Corey, Colorado State University Hydrology Paper No. 3 (1964).
5. C. McPhee, J. Reed, I. Zubizarreta, Core Analysis: A Best Practice Guide, Elsevier (2015).
6. L. Zuo, S. Krevor, R.W. Falta, S.M. Benson, Transport in Porous Media, 91(2), 459–478 (2012).
7. C.A. Reynolds, S. Krevor, Water Resources Research, 51(12), 9464–9489 (2015).
8. J.-C. Perrin et al., Energy Procedia, 1(1), 3515–3522 (2009).
9. S. Bachu, Energy Procedia, 37, 4428–4436 (2013).
10. X. Chen, D.A. DiCarlo, Advances in Water Resources, 96, 251–265 (2016).
11. A. Busch, N. Mueller, Energy Procedia, 4, 6053–6060 (2011).
12. R. Czarnota et al., ARMA-2022-0435 (2022).
13. M. Akbarabadi, M. Piri, Advances in Water Resources, 52, 190–206 (2013).
14. S. Berg, S. Oedai, H. Ott, International Journal of Greenhouse Gas Control, 12, 478–492 (2013).
15. G.S. Jeong, J. Lee, S. Ki, D.-G. Huh, C.-H. Park, Energy, 133, 62–69 (2017).
16. S. Bachu, B. Bennion, Environmental Geology, 54, 1707–1722 (2008).
17. Y. Sun, L. Wei, C. Dai, Z. Yu, Y. Xin, Chemical Geology, 584, 120527 (2021).
18. G.S. Jeong, S. Ki, D.S. Lee, I. Jang, Sustainability, 13, 1543 (2021).
19. B. Bennion, S. Bachu, SPE-99325-MS (2006).
20. C. Reynolds, M. Blunt, S. Krevor, Energy Procedia, 63, 5577–5585 (2014).
21. G.-B. Seok, Y.-C. Park, J.Y. Lee, Y.-K. Lee, K.-Y. Kim, H. Son, M. Raab, Energy Reports, 9, 3755–3770 (2023).
22. D.B. Bennion, S. Bachu, SPE-106995-MS (2007).
23. R. Farokhpoor, E.G.B. Lindeberg, O. Torsaeter, M.B. Mork, A. Mork, Greenhouse Gases: Science and Technology, 4, 36–52 (2014).
24. J. Moore, P. Holcomb, D. Crandall, S. King, J.-H. Choi, S. Brown, S. Workman, Advances in Water Resources, 153, 103953 (2021).
25. B. Bennion, S. Bachu, SPE-95547-MS (2005).
26. X. Chen, A. Kianinejad, D.A. DiCarlo, SPE-169137-MS (2014).
27. H. Darcy, Les fontaines publiques de la ville de Dijon, Victor Dalmont, Paris (1856).
28. L.J. Klinkenberg, API Drilling and Production Practice, 200–213 (1941).
29. W. Tanikawa, T. Shimamoto, International Journal of Rock Mechanics and Mining Sciences, 46(2), 229–238 (2009).
30. T. Orlander et al., Journal of Petroleum Science and Engineering, 169, 552–561 (2018).

31. G. Soave, Chemical Engineering Science, 27(6), 1197–1203 (1972).
32. N. Spycher, K. Pruess, Transport in Porous Media, 82(1), 173–196 (2010).
33. S. Whitaker, Transport in Porous Media, 1(2), 105–125 (1986).
34. M. Ayub, R.G. Bentsen, Journal of Petroleum Science and Engineering, 23(1), 13–26 (1999).
35. A. Ahmed, S. Ahmed, A. Keshavarz, S. Iglauer, K. Zhang, A. Saeedi, SPE-220889-MS (2024).
36. R. Chai, S. Bultreys, D. Avraam, Z. Yang, S. Singh, B. Bijeljic, M.J. Blunt, Transport in Porous Media (2026).
37. J.D. Walls, J. Reed, E.H. Ahmed, A. Mitra, SPE/AAPG/SEG CCUS-2025-4184007 (2025).